Climate Dynamics
https://doi.org/10.1007/s00382-024-07252-9

ORIGINAL ARTICLE

Escalation of tropical cyclone impacts on the northwestern Bay of Bengal over the past decade

Dijia Wu[1,3] · Xia Ju[1,2,3] · Jia Sun[1,2,3,4] · Xiaomin Hu[1] · Xuejun Xiong[5]

Received: 8 December 2023 / Accepted: 20 April 2024

Abstract
Tropical cyclones have resulted in casualties and economic losses in the areas surrounding the Bay of Bengal (BoB). Thus, a comprehensive investigation of these tropical cyclones holds vital implications for disaster preparedness and mitigation. This paper compares the occurrence of storms in the last two decades, i.e., 2002–2011 and 2012–2021, and results reveal that such storms exhibited predominantly a northwesterly track towards the northwestern BoB, with a severer intensity but equal total storm frequencies. Over the past decade, a southeast-northwest pathway (SNP) was identified, demonstrating a higher incidence of severe tropical cyclones (STC, with lifetime maximum intensity ≥ 64 knots) over the BoB. Further analysis of the changes in the environmental conditions between these two decades indicates that a southeasterly anomaly in the steering flow contributed to the formation of the SNP. During the same period, the more favorable oceanic conditions during the last decade, including higher sea surface temperatures, a greater upper ocean heat content, a thicker warm water layer, and a thicker barrier layer beneath the SNP, favored the development of these storms by providing more heat energy to the storms. The atmospheric conditions, including increased air-sea heat fluxes, moisture, and instability within the lower troposphere, as well as reduced vertical wind shear, facilitated the development of convection within these storm systems. These favorable conditions improved the potential for storm development into STCs and elevated the risk of the northwestern BoB being impacted by more destructive storms.

Keywords Tropical cyclone · Bay of Bengal · Climate change · Large-scale environments

1 Introduction

A tropical cyclone is a low-pressure system which forms over warm ocean surfaces and is characterized by strong winds and heavy precipitation. The tropical cyclones in the northern Indian Ocean (NIO) account for only 6–7% of the global total amount (Neumann 2017; Sahoo and Bhaskaran 2016), but the loss of life resulting from these tropical cyclones and their derived disasters ranks among the highest globally (Peduzzi et al. 2012). Compared to the Arabian Sea, the oceanic and atmospheric conditions in the Bay of Bengal (BoB) are more conducive to the formation of tropical cyclones (Deshpande et al. 2021; Mohapatra and Kumar 2017). This advantage, together with the westward propagation of disturbances in the western North Pacific Ocean, results in 2–4 times the number of tropical cyclones occurring in the BoB compared to the Arabian Sea (Duan et al. 2021; Wahiduzzaman and Yeasmin 2020). The South Asian summer monsoon has a strong influence on the tropical cyclones in the BoB, restraining their formation and

Dijia Wu and Xia Ju are listed as co-first authors and contributed equally to this work.

✉ Jia Sun
sunjia@fio.org.cn

1 First Institute of Oceanography, and Key Laboratory of Marine Science and Numerical Modeling, Ministry of Natural Resources, Qingdao 266061, China

2 Laoshan Laboratory, Qingdao 266237, China

3 Shandong Key Laboratory of Marine Science and Numerical Modeling, Qingdao 266061, China

4 College of Ocean Science and Engineering, Shandong University of Science and Technology, Qingdao 266590, China

5 Institute of Physical Oceanography and Remote Sensing, Ocean College, Zhejiang University, Zhoushan 316021, China

Published online: 10 May 2024

development during the onset period through the combined effects of intense vertical wind shear and other atmospheric parameters (Duan et al. 2021; Li et al. 2013; Yanase et al. 2012). Consequently, the annual frequency of tropical cyclones in the BoB exhibits a distinctive bimodal pattern, with peaks occurring in the pre-monsoon (April–May) and post-monsoon (October–December) seasons, and the latter season exhibiting a higher peak due to seasonal variability of the relative humidity (Deshpande et al. 2021; Gray 1968; Li et al. 2013). Data compiled by the Emergency Events Database (EM-DAT) indicates that since 1952, tropical cyclones have affected 237 million people and caused economic losses of US $76 million in the countries and regions around the BoB (Fig. 1). A comprehensive study of tropical cyclones holds vital implications for disaster preparedness and mitigation in the vicinity of the BoB.

In the context of global warming, tropical cyclones over some basins have exhibited some similar trends. Previous studies have reported a decreasing frequency over the Western North Pacific Ocean and the Southern Indian Ocean, as well as an increasing frequency over the North Atlantic Ocean and central Pacific Ocean (Hsu et al. 2014; Liu and Chan 2013; Murakami et al. 2020). In most basins, tropical cyclones have intensified in recent decades, and their occurrence and propagation have exhibited ongoing poleward migration (Emanuel and Nolan 2004; Kim et al. 2020; Kossin et al. 2013, 2014; Shan and Yu 2021; Sun et al. 2017). The data inconsistency caused by changes in long-term measurement practices leads to uncertainty regarding how the translation speed of global tropical cyclones has changed (Chan 2019; Kossin 2018).

Regarding tropical cyclones over the BoB, Balaguru et al. (2014) investigated the storm seasons from 1981 to 2010 and determined that the ocean and atmospheric conditions became more favorable for the growth of tropical cyclones in the post-monsoon season, which led to intensification of the tropical cyclones. Deshpande et al. (2021) conducted a comparative analysis of NIO cyclones between the late 20th century and the early 21st century. They found that there was an 8% decrease in the frequency of relatively weak cyclones, and the duration of the tropical cyclones over the BoB in November exhibited a decreasing trend. However, the genesis location and accumulated cyclone energy (ACE) did not exhibit specific changes. Sun et al. (2021) examined the relationship between the translation speed and intensity in the BoB, revealing a higher decrease in the translation speed for intense cyclones compared to weaker ones.

Under the current scenario of climate change, the countries along the northwestern coast and the mouth of the BoB are experiencing more frequent storm landfall and precipitation events (Kabir et al. 2022; Shrivastav et al. 2022; Yuan and Cao 2013). However, the reason for this shift in storm activities remains unclear. Previous studies have indicated that the initial depressions of storms tend to form over warm sea surfaces with positive vorticity anomalies and their motion is driven by the large-scale steering flow (Gray 1979; Krishnamohan et al. 2012; Wu and Wang 2004). In addition, storms obtain energy and moisture from favorable ocean and atmospheric conditions to develop cloud systems and strengthen wind fields. The migration of storm tracks is primarily attributed to changes in the genesis location and large-scale circulation patterns, while the storm intensity is dominated by the oceanic and atmospheric environments. The goals of this study were to address the following questions: Have the environmental conditions in the BoB changed? What is the relationship between the changes and the increasingly frequent storm events in the northwestern BoB?

The remainder of this paper is organized as follows. The datasets and methods are described in Sect. 2. Section 3 presents analyses of the changes in the characteristics of tropical cyclones in the BoB over the past 20 years, affirming the findings of previous research. In Sect. 4, we discuss the factors influencing storm activities and related mechanisms. A summary and discussion are presented in Sect. 5.

2 Data and methodology

2.1 Data

The storm data for the BoB were obtained from the Joint Typhoon Warning Center (JTWC) dataset developed by the International Best Track Archive for Climate Stewardship (IBTrACS, Version 4). This dataset includes the location, time, maximum of the 1 min averaged sustained wind speed, minimum central pressure, and wind radii at each observation time. The observations were conducted at intervals of 3 to 6 h (Knapp et al. 2010, 2018). The storms that occurred in the BoB (75–100°E, 0–25°N, the area indicated by the magenta rectangular box in Fig. 1, from 2002 to 2021 that had a maximum sustained wind speed (MSW) of 34 kt or greater for more than 12 h were considered in the analysis. A total of 60 storm events were obtained. The formation time of the storms used in this study was defined as the time when the storm reached 34 kt. For statistical convenience, we classified the 60 storms, based on their lifetime maximum intensities (LMI), as tropical cyclones (TCs, LMI $\leq$ 63 kt) and severe tropical cyclones (STCs, LMI $\geq$ 64 kt). Since the storms that occurred during April–May and October–December accounted for 93% of these 60 storms, these months were defined as the cyclogenesis season.

The sea surface temperature (SST) data were obtained from the Remote Sensing Systems (RSS) and were

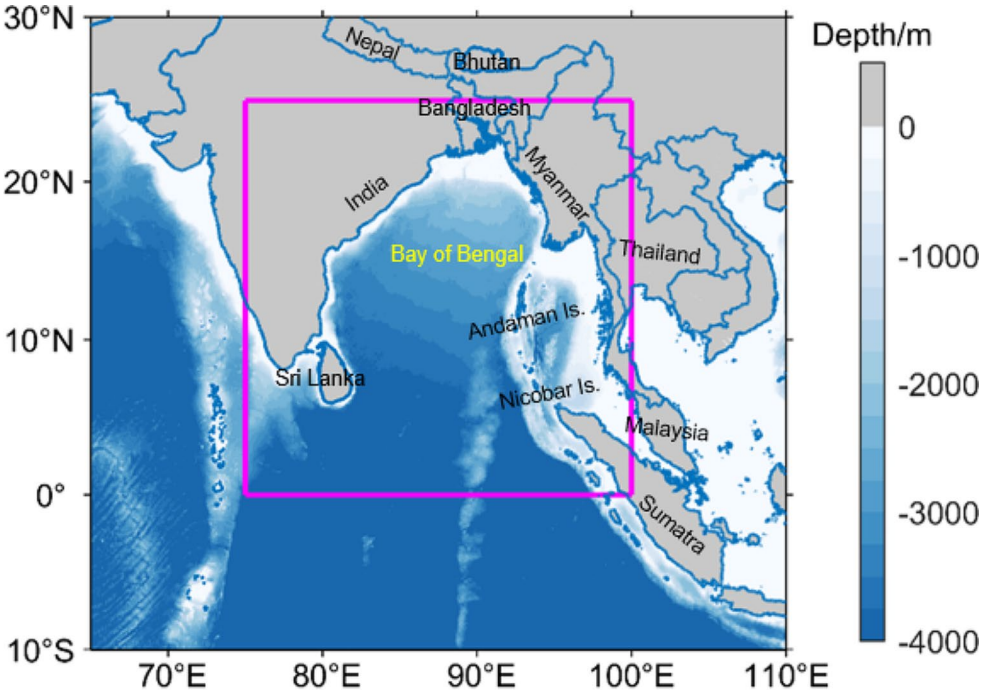

Fig. 1 The BoB Basin and its bordering countries. The magenta rectangular box indicates the actual study area where storms were tracked. The colors in the body of water represent the water depth. The Etopo2 data were provided by the National Geophysical Data Center (2006)

optimally interpolated using high-resolution satellite microwave imager (MW) and infrared radiometer (IR) observations (Wentz et al. 2015). This daily product is available from June 2002 to the present with a 9 km × 9 km spatial resolution.

The ocean elements data were derived from the Global Ocean Argo gridded dataset (BOA_Argo, Version 2020), including the global monthly mean temperature, salinity, mixed layer depth, and isothermal layer depth. This product covers the period from 2004 to 2022, with a spatial resolution of 1° × 1° in the horizontal direction and 58 levels in the vertical direction from the surface to 1975 dbar (Li et al. 2017).

The atmospheric elements data were obtained from National Centers for Atmospheric Prediction/National Center for Atmospheric Research (NCEP/NCAR) Reanalysis 1 Project (Kalnay et al. 1996), and these data were derived from a combination of observations and model simulations. Data are available from 1945 to the present with a spatial resolution of 2.5° × 2.5° in the horizontal direction and 17 levels in the vertical direction. In this study, the monthly mean wind, specific humidity (SH), 500 hPa geopotential height (H_{500}), and air temperature data were used. All of the data used in this study were from 2002 to 2021.

2.2 Methods

To quantify the spatial changes in the storm frequencies over the BoB, the basin is divided into four quadrants (henceforth Q1 to Q4) that intersected at 89°E, 12.5°N (Fig. 2c). In this study, ACE is defined as the sum of kinetic energy of storms within the same spatial quadrant, computed using square of MSW of storms in each quadrant. The calculation is based on Camargo and Sobel (2005):

$$ACE = 10^{-4} \sum V^2, \tag{1}$$

where V is the MSW of each storm.

The steering flow is calculated as the average wind field from 850 to 300 hPa (Sun et al. 2019; Wu and Wang 2004).

As reported by Leipper and Volgenau (1972), 26 °C is seen as the temperature below which storms do not form and the mean tropical atmospheric temperature during storm season. Therefore, the depth of the 26 °C isotherm (D26) and the upper ocean heat content (UOHC) are commonly used to measure the thermal structure of the upper ocean associated with storms (Deshpande et al. 2021; Kashem et al. 2019; Leipper and Volgenau 1972). D26 is expressed as the depth at which the interpolated Argo sea temperature data are the closest to 26 °C. The UOHC is calculated using the vertical integral of the sea temperature values above 26 °C via previously developed methods as follows (Chih and Wu 2020; Kashem et al. 2019; Leipper and Volgenau 1972):

$$UOHC_{(x,y)} = \rho C_p \int_{z=0}^{D26} (T_{(x,y,z)} - 26) dz, \tag{2}$$

where the density of sea water is set as ρ = 1026 kg m^{-3}, and the heat capacity at a constant pressure is C_p= 4178 J kg^{-1} °C^{-1}. The integration is performed from z = 0 to D26, and $T_{(x,y,z)}$ represents the sea temperature at a horizontal location (x, y) and depth z.

In the BOA_Argo dataset, the isothermal layer depth (D_1) and isopycnal layer depth (D_2) are calculated using the maximum angle method. In a certain grid, $D_1 > D_2$ indicates the presence of the barrier layer. The barrier layer thickness (BLT) is calculated as $BLT = D_1 - D_2$, and the mixed layer depth (MLD) is defined as $MLD = D_2$. Conversely, if $D_1 < D_2$, the compensated layer (CL) is present. The compensated layer thickness (CLT) is computed as $CLT = D_2 - D_1$, and $MLD = D_1$.

The vertical wind shear (VWS) is calculated as the difference in the wind speed between the 850 hPa and 200 hPa levels using the method of (Deshpande et al. 2021):

$$VWS = \sqrt{(u_{200} - u_{850})^2 + (v_{200} - v_{850})^2}, \quad (3)$$

where u_{200} and u_{850} are the zonal wind speeds at the 200 hPa and 850 hPa pressure levels, respectively. Similarly, v_{200} and v_{850} are the meridional wind speeds at the 200 hPa and 850 hPa pressure levels.

The moist static energy (MSE) is used to represent the sum of the internal energy, potential energy, and latent heat in moist air. The calculation formula is as follows (Balaguru et al. 2014; Deshpande et al. 2021):

$$MSE = C_p T + gz + L_v q, \quad (4)$$

where the specific heat capacity of dry air at constant pressure is C_p= 1.005 kJ kg^{-1} K^{-1}, the latent heat of condensation is L_v= 2256 kJ kg^{-1}, T is the air temperature, and q is the SH. In this study, MSE is defined as the average value between the 700 hPa and 925 hPa pressure levels.

3 Observed changes in storm characteristics

Figure 2a–b display the storm occurrence in the BoB Basin during 2002–2011 and 2012–2021, respectively, and the changes in the storm frequencies are compared in Fig. 2c. The results show a lack of storm movement in a northwesterly direction and the occurrence of few storms, especially in the region near 82°E, 15°N during the first decade (Fig. 2a). Most of the storms, including three super cyclone storms (SuCS, LMI ≥ 120 kt in the NIO classification) preferentially moved westward or north-northeastward, making landfall over southeastern India, Bangladesh, and Myanmar coast (Fig. 1a). During the second decade, a distinct increase was observed in the northwestward moving storms, and consequently, the storm occurrence frequency was higher in the northwestern BoB (Fig. 2c). It should be noted that more storms reached the level of very severe cyclone storms (VSCS, 64–119 kt) or higher intensity in the second decade (Fig. 2b). In this paper, the spatial distribution of the quantity of storm centers on a 0.5° × 0.5° grid is calculated during each decade, and the difference between the two decades is shown as Fig. 2c. The results illustrate that more storm centers occurred in Q2 and fewer occurred in Q1 and Q3,

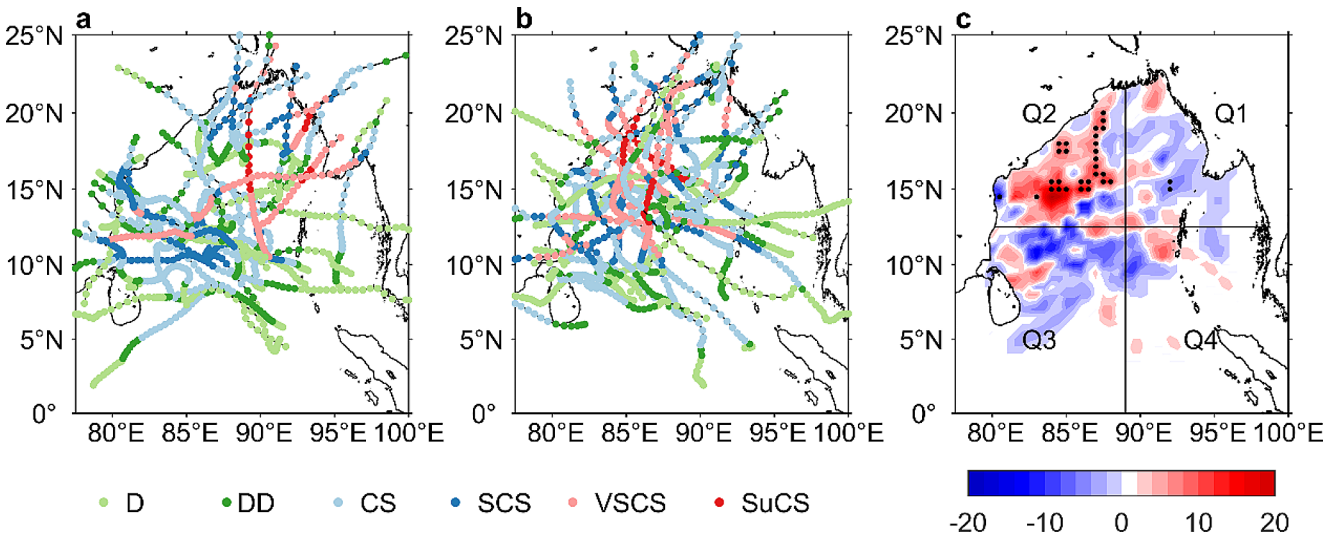

Fig. 2 Storm occurrence over the BoB during **a**) 2002–2011 and **b**) 2012–2021. **c**) Difference in quantity of storm center distribution on 0.5° × 0.5° grids. The BoB was divided into four quadrants with an intersection at 89°E, 12.5°N. D, DD, CS, SCS, VSCS, SuCS are abbreviations for traditional tropical cyclone classifications in the NIO. They respectively refer to depression (1–27 kt), deep depression (28–33 kt), cyclone storm (34–47 kt), severe cyclone storm (48–63 kt), very severe cyclone storm (64–119 kt), and super cyclone storm (≥ 120 kt). The dotted areas pass the significance test at 90% confidence level

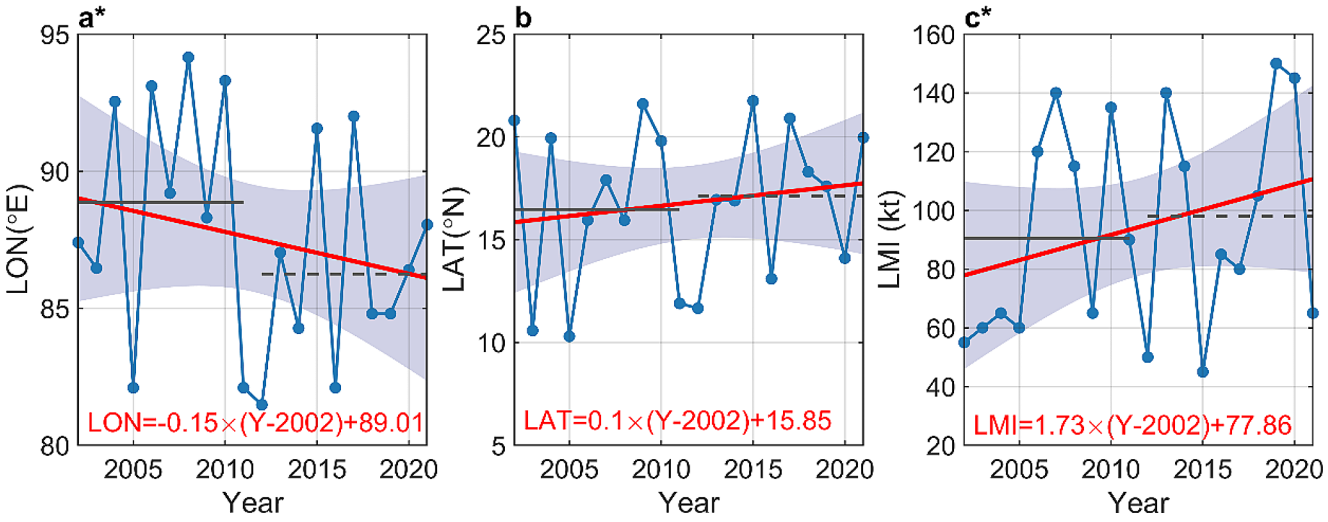

Fig. 3 Time series (blue lines), decadal averages (gray lines, solid and dashed lines represent the 2002–2011 and 2012–2021 periods, respectively), and linear fitting results (red lines and equations) with 95% two-sided bounds (shaded areas) of **a**) longitudes, **b**) latitudes, and **c**) LMIs of the strongest storms in each year. Asterisks after the ordinals represent that the trends pass the significance test at 95% confidence level

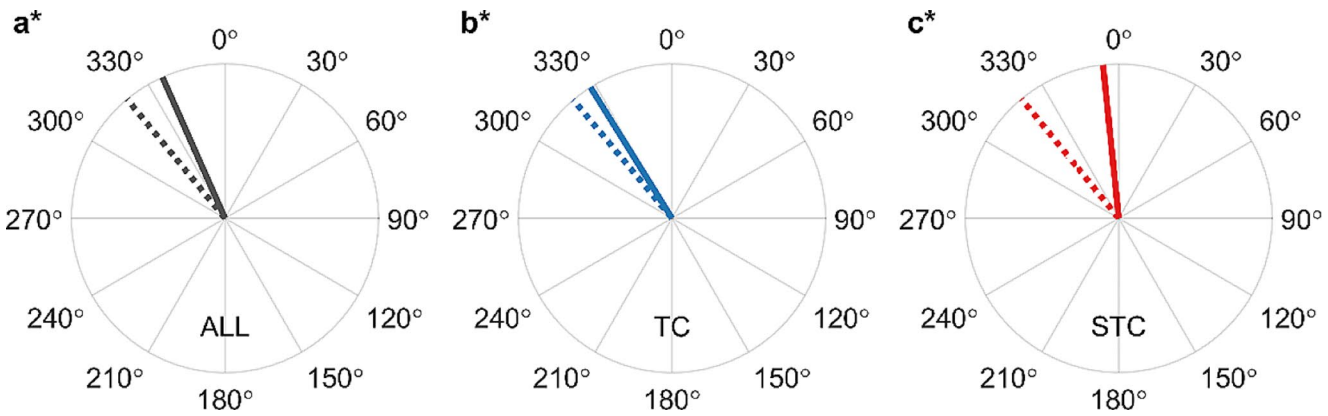

Fig. 4 Comparisons of the mean translation direction (unit: °) of **a** all of the storms, **b**) TCs, and **c**) STCs between each decade. The solid and dashed lines represent the averages of the 2002–2011 and 2012–2021 periods, respectively. Asterisks after the ordinals represent that the changes in the variables pass the significance test at 95% confidence level

and a southeast-northwest pathway (SNP), which was narrow in Q4 and wide in Q2, developed (Fig. 2c).

Figure 3 displays the time series, average values and trends of the spatial positions, as well as the LMIs, of the storms with the strongest intensity each year. During 2002 − 2011, storms achieved their LMIs at an average longitude of 88.9°E, while in the subsequent decade, the average longitude was 86.3°E, shifting westward by 2.6° (Fig. 3a). The reduction in longitudes at which storms achieved their LMIs was approximately $-0.15 \pm 0.16°$ per year. During the same period, the average latitude migrated northward by 0.6°, from 16.5°N to 17.1°N (Fig. 3b). The latitudes at which storms achieved their LMIs increased by approximately $0.1 \pm 0.15°$ per year. These results indicate a northwestward migration of storm LMIs. Over the two decades, the decadal mean LMI increased from 90.5 kt to 98 kt, and the annual LMI increased at a rate of 1.73 ± 1.37 kt per year (Fig. 3c). The increase in LMIs constituted a greater threat to the BoB.

On average, the storms in the BoB moved in a northwestward direction (Fig. 4). However, the storms during the first decade moved towards the north-northwest, whereas the direction of those during the latter decade significantly diverted westward compared to those during the former decade. Moreover, the diversion degree of the STCs was larger than that of the TCs, suggesting the existence of the SNP.

Figure 5 shows the time series of the storm frequency, duration, and translation speed. As can be seen in Fig. 5a–c, a total of 21 TCs and nine STCs were observed in the first decade compared to 16 TCs and 14 STCs in the second decade. The frequencies of the TCs and STCs decreased by

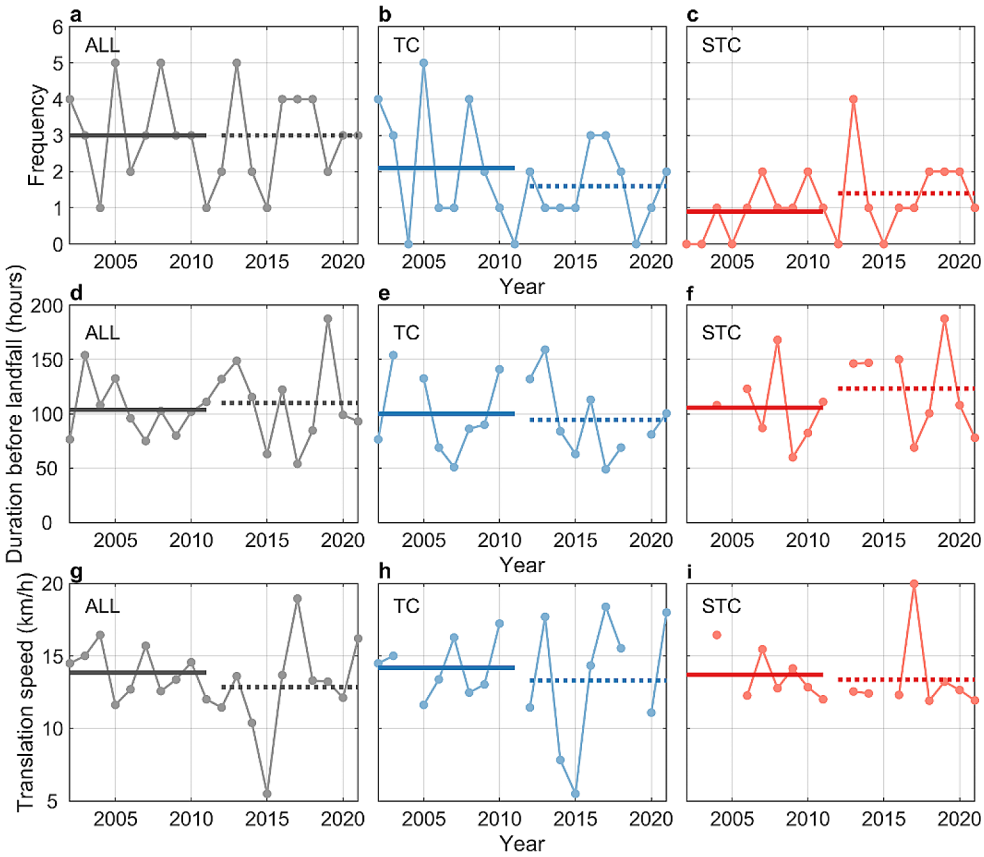

Fig. 5 Time series of the **a–c**) frequency, **d–f**) mean duration before landfall of each storm, and **g–i**) mean translation speed of all storms, TCs, and STCs in each year. The solid and dashed lines denote the averages for the 2002–2011 and 2012–2021 periods, respectively

23.8% and increased by 55.6%, respectively. STCs occurred more frequently. In terms of the total storm duration, the second decade experienced an appreciable increase, especially in the STC duration, suggesting a longer storm activity period. The duration increased from 3126 h (including 2217 h attributed to TCs and 909 h attributed to STCs) in the first decade to 3297 h (TCs accounting for 1476 h and STCs accounting for 1821 h) in the second decade. Since the total duration may be influenced by the storm frequency, the mean duration for a single storm was calculated (Fig. 5d–f). The decadal averages of the TCs and STCs were relatively similar during 2002–2011. Then they insignificantly decreased by 5.5% and increased by 16.7%, respectively, during 2012–2021, and the average duration of the STCs became longer than that of the TCs. The translation speed of a storm affects its duration. As displayed in Fig. 5g, the average translation speed of storms exhibits insignificant decrease during the two decades. For TCs, they moved at an average speed of 14.2 km/h during 2002–2011 and 13.3 km/h during 2012–2021, which slowed down by 0.9 km/h in the latter decade (Fig. 5h). For STCs, their average translation speed declined by 0.3 km/h, from 13.7 km/h during 2002–2011 to 13.4 km/h during 2012–2021 (Fig. 5i). The slower speed prolonged their duration on the sea, allowing them to gather more energy and ultimately achieve higher LMIs.

Figure 6 and Table 1 show the time series and decadal averages of the ACE of the storm centers in the four quadrants. It can be seen that the storm centers were mainly active in Q1, Q2, and Q3. Notable changes occurred between Q1 and Q2, in which the main contributor to the ACE was STCs. In the first decade, Q1 had a high frequency and intensity of STC centers, while Q2 mostly contained TC centers. In the second decade, the STC centers shifted from Q1 to Q2, leading to a significant increase in the ACE in Q2. The enhanced ACE in Q2 was also derived from Q3. The ACE in Q3 was mainly generated by TC centers. They migrated to Q2 during 2012–2011, but their original quantity and intensity were not sufficient to account for the entire increase in the ACE, suggesting that they transformed into more intense STC centers. In the later years of the second decade, there was an increase in the occurrence of STC centers in Q3, but their energy was not high enough to significantly influence the local ACE. In Q4, the frequency of TC centers remained relatively stable over the two periods, while the STC centers were minimal and had a lower intensity in the second decade, contributing to the overall decreasing trend of the ACE. The statistical results indicate that Q2 gained storm centers that migrated and transformed from Q1 and Q3 in the second decade, leading to a significant increase in its ACE. Based on the above results, the storms in the BoB did indeed become more intense and shifted northwestward.

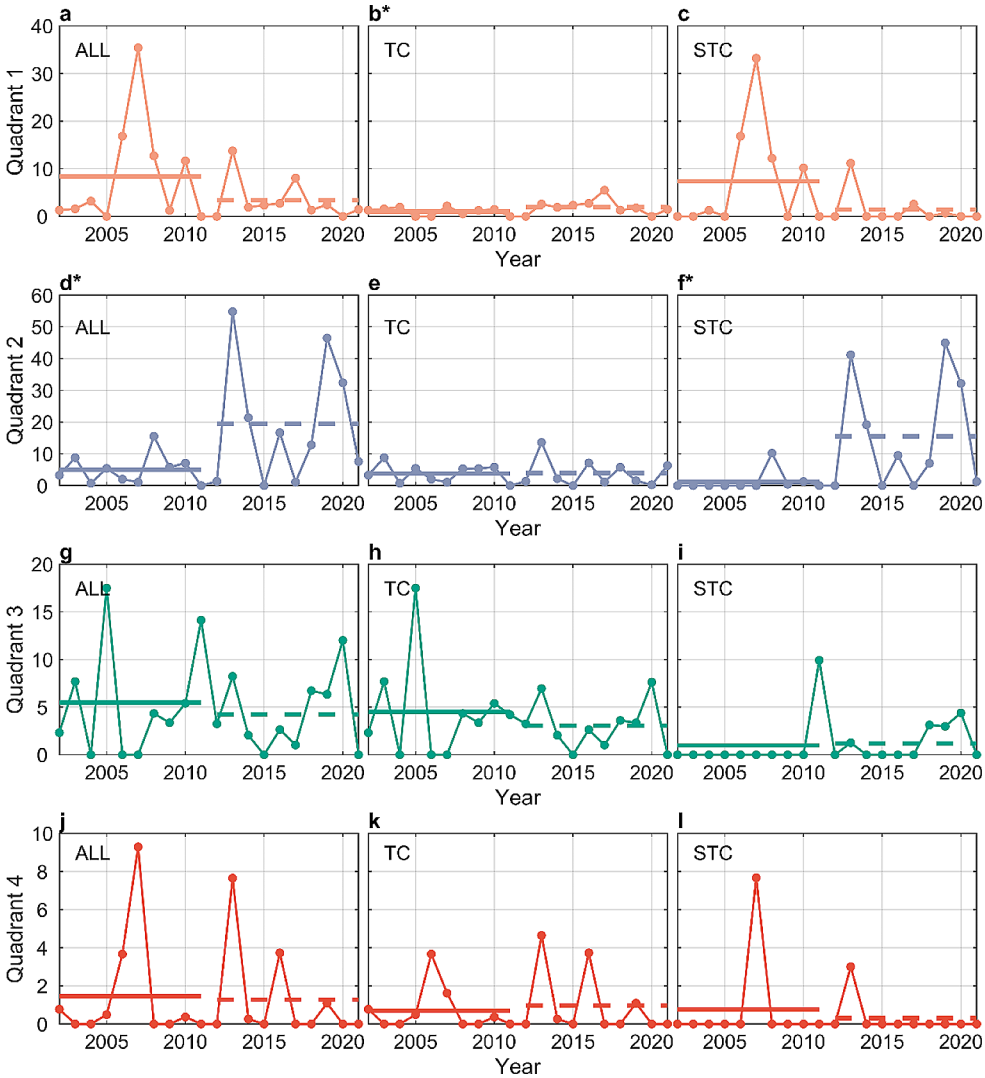

Fig. 6 Time series of ACE (unit: kt^2) of storm centers in **a–c**) Q1, **d–f**) Q2, **g–i**) Q3, and **j–l**) Q4 in the BoB Basin. TC and STC denote storm centers with intensities of 34–63 kt and ≥ 64 kt, respectively. The solid and dashed lines denote the averages of the 2002–2011 and 2012–2021 periods, respectively. Asterisks after the ordinals represent that the changes in the variables pass the significance test. Among them, the changes in All ACE and STC ACE in Q2 reached the 95% significance level, and the changes in TC ACE in Q1 reached the 90% significance level

Table 1 Decadal averages of ACEs (unit: kt^2) of storm centers in each quadrant

	All		TC		STC	
Quadrant	2002–2011	2012–2021	2002–2011	2012–2021	2002–2011	2012–2021
1	8.4	3.4	1.03	1.97	7.37	1.44
2	4.98	19.45	3.79	3.93	1.19	15.53
3	5.47	4.23	4.48	3.05	0.99	1.18
4	1.46	1.27	0.69	0.97	0.77	0.3

4 Mechanism analysis

4.1 Storm track transition

The tracks of storms depend on their genesis locations and the large-scale steering flow, which is usually represented by the average wind field between the 850 hPa and 300 hPa levels in the atmosphere (Wu and Wang 2004). To analyze the concrete reasons for the storm translation changes, we investigated the storm genesis locations, decadal average steering flow, and 500 hPa geopotential height during the two decades. As shown in Fig. 7, in the first decade, the storm genesis locations were dense in Q4 and sparse in the other quadrants; while in the second decade, westward and northward migration of the storm genesis locations in Q4 occurred, which may have led to the translation of the storm tracks. Additionally, during the cyclogenesis season, easterlies prevailed in the equatorial region and the prevailing winds shifted to westerly north of 15°N. Of particular interest is that the equatorial westerlies strengthened and a cyclonic circulation anomaly (CCA) appeared in Q3, while an anticyclonic circulation anomaly (ACA) appeared in Q1

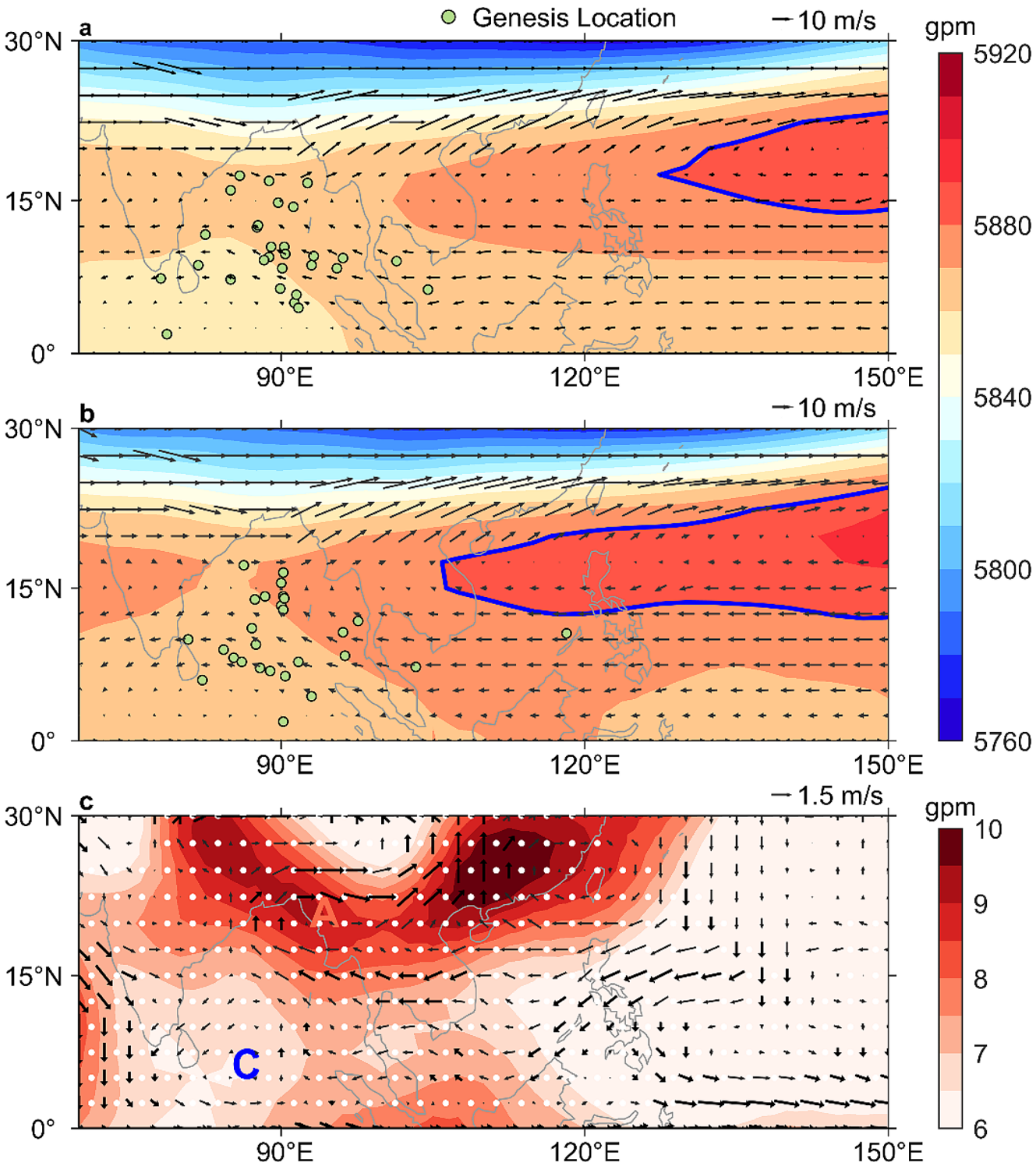

Fig. 7 Genesis location of storms (circles), decadal average steering flow (unit: m/s; vectors) and 500 hPa geopotential height (unit: gpm; color) in cyclogenesis season during **a**) 2002–2011 and **b**) 2012–2021. The blue lines indicate the 5880 gpm lines. **c**) Changes in geopotential height and steering flow between the two decades. A and C denote anticyclonic and cyclonic circulation anomalies, respectively. The dotted areas represent the geopotential height anomalies exceed the 95% significance level, and thick vectors represent steering flow whose zonal and meridional components exceed the 90% significance level

in the second decade (Fig. 7c). The CCA and ACA facilitated and suppressed the formation of the storms in their respective regions of influence to some extent. The presence of the CCA and ACA also induced a southeast anomaly across them both, which played a considerable role in the formation of the SNP. Around the CCA, the newly generated storms could be pushed northward by the enhanced southerlies in front of the CCA, and then, they entered the SNP. Similarly, the enhanced easterlies at the bottom of the ACA could push the storms formed in the northern BoB into the SNP. Along the SNP, the storms were more likely to move towards the northwestern coast of the BoB with the help of the strengthened southeast anomaly, resulting in the increase in tropical cyclone impacts on the northwestern BoB over the second decade.

Previous studies have revealed that global warming has a significant lifting effect on geopotential height (Dong et al. 2023; Yang et al. 2022; Zhang et al. 2021). As shown in Fig. 7, above the BoB H_{500} increased during 2012–2021, and it increased more in Q1 and less in Q3. This asymmetrical distribution resulted from the westward intensification of the western Pacific subtropical high (WPSH), which is expressed by the position of 5880 gpm contour (blue lines in Fig. 7a–b) and can be modulated by the Pacific Decadal Oscillation (PDO) (Feng et al. 2014; Liu et al. 2019; Qin et al. 2024; Xu et al. 2019). Earlier studies showed that the west boundary of WPSH in warm PDO phase is further west during the positive (warm) phase than that during the negative (cold) PDO phase (Feng et al. 2014; Liu et al. 2019; Qin et al. 2024; Xu et al. 2019). This is because, compared with the negative PDO phases, the warmer Indian Ocean with stronger convection, as well as the associated heating effect, is more favorable to the westward extension of the WPSH during the positive PDO phase (Liu et al. 2019). Consequently, the PDO phase during 2002–2021 deserves consideration. Figure 8 shows the monthly PDO index for the two decades provided by the Tokyo Climate Center (2023). During 2002–2005, the PDO was in a relatively weak positive (warm) phase, which was followed by a negative (cool) phase from 2006 to 2013 (with a short interruption during the moderate El Niño event during 2009–2010). Then, the PDO changed to a positive (warm) phase in 2014 and remained in this phase until 2020. The phase change of the PDO in the first decade kept the Indian Ocean relatively cool; therefore, the steering flow affected by H_{500} did not favor the northwestward translation of storms (Fig. 7a). In the second decade, the second phase change of the PDO induced warming of the Indian Ocean and subsequently the westward extension of the WPSH, resulting in higher H_{500} over the eastern Indian Ocean–western North Pacific Ocean (Fig. 7b). The ACA formed in the area with higher geopotential heights, and a southeast anomaly formed on the outside of the ACA (Fig. 7c). Overall, the asymmetrical increasing pattern of H_{500} modulated by the negative-to-positive phase change of the PDO during the second decade contributed to the formation of the southeast anomaly in the large-scale steering flow.

4.2 Storm intensity

Both environmental oceanic and atmospheric conditions play important roles in the development of storms (Balaguru et al. 2014; Deshpande et al. 2021; Sun et al. 2022). Therefore, the changes in oceanic environments, including the SST, D26, UOHC, and BLT, and in atmospheric environments, including the air-sea heat fluxes, SH, VWS, and MSE, and their effects on storm development are analyzed in this section.

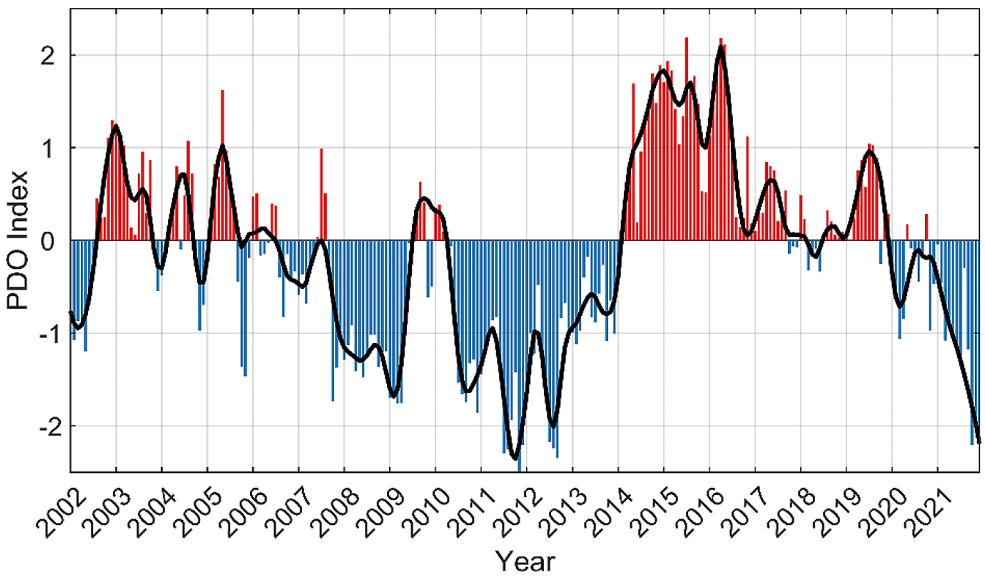

Fig. 8 The monthly PDO index during 2002–2021. The red bars indicate positive (warm) phases; the blue bars indicate negative (cool) phases; and the black line indicates the smoothed values

4.2.1 Sea surface temperature

Figure 9 displays the spatial distribution of the SST in the cyclogenesis season in the BoB averaged over the two-decade period and their differences. The results show that there were poleward and westward decreasing spatial patterns during these two periods (Fig. 9a–b). The averaged SSTs in the BoB were both > 27 °C, and they exceeded 28.8 °C and 29.0 °C south of 15°N in the two decades, respectively. This provided favorable conditions for TC development during these two periods. By 2012–2021, the SST beyond the mouth of the BoB had significantly increased by 0.2 °C, and the SST in the area extending from southern Sri Lanka to the Andaman Sea experienced warming of 0.3 °C (Fig. 9c). This warming was even greater along the eastern and western coastal areas. The higher SST in the second decade could contribute a greater surface heat flux from the ocean to the storms and was more favorable for the development of storms.

4.2.2 Depth of 26 °C isotherm

As storms pass over the ocean, they entrain a great deal of heat from the upper warm water layer and induce vertical mixing of the seawater, causing upwelling, which decreases the SST and weakens the storms (Emanuel 1999). Therefore, the thickness of the warm water layer significantly influences the growth and maintenance of the storms. Represented by D26, the thickness of the warm water layer during the two decades and their difference are shown in Fig. 10. In the BoB, the average D26 ranged from 60 to 90 m, presenting a pattern of shallow in the west and deep in the east and near the equator. The thicker warm water layer near the equator was the result of downwelling Kelvin waves triggered by westerly winds above the sea surface (Balaguru et al. 2014; Girishkumar and Ravichandran 2012; Sreenivas et al. 2012). In the northeastern BoB, the interaction between the anticyclonic eddies and wind stress can lead to upwelling at the center of the anticyclonic eddies (McGillicuddy 2015; Zhou et al. 2022). Due to Rossby waves radiating from the Kelvin waves, the anticyclonic eddies propagated in a westward direction (Cui et al. 2022). As a result, the warm water extended westward and generated a warm tongue around 15°N. In the second decade, enhanced westerly winds (Fig. 7) caused deepening of the equatorial D26 by approximately 10 m and the D26 in the SNP by 1–3 m. Although in certain areas beyond the SNP, D26 exhibited a decrease, the D26 in the SNP was > 70 m, making it harder for deep cold water to be pumped to the upper layer through vertical mixing.

4.2.3 Upper ocean heat content

The UOHC during the two decades and their differences are displayed in Fig. 11. The UOHC in the BoB ranged from 40 to 100 kJ/cm^2 and was greater in the southeast and lower in the northwest. Affected by the distribution of D26, the higher UOHC region around the Andaman Islands extended westward. Compared to the first decade, during the second decade, the UOHC increased over the entire basin. The equatorial region experienced the greatest enhancement, followed by the western coast of the BoB and the western part of the Andaman Islands. Similar to the D26, the westerly wind anomalies near the equator further triggered

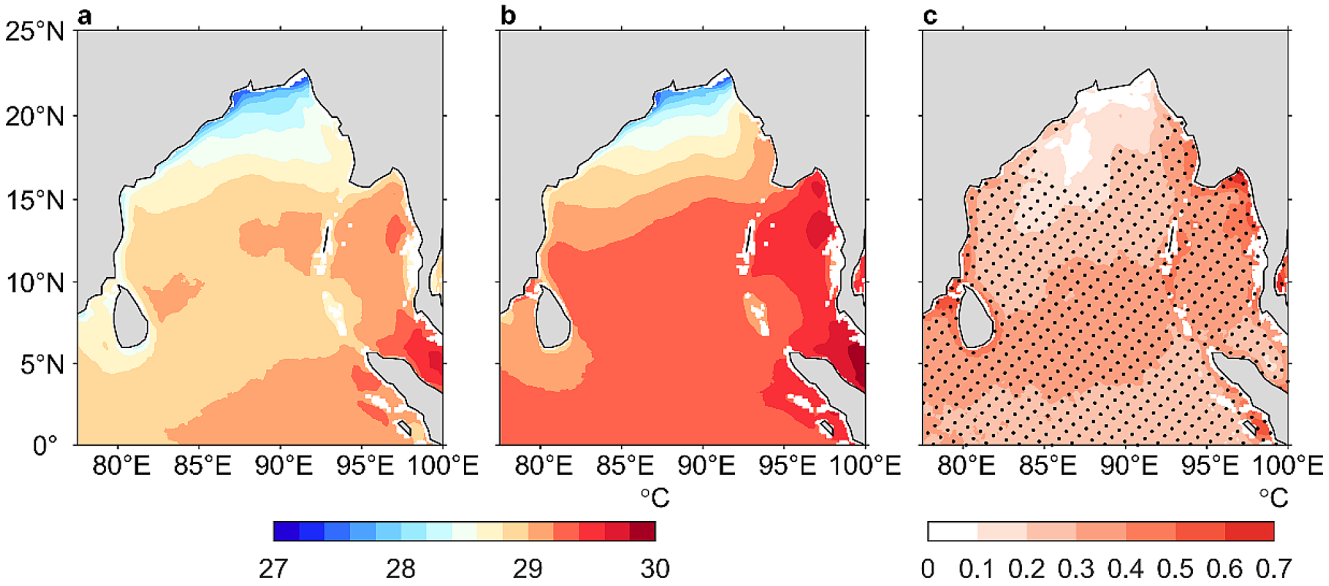

Fig. 9 Spatial distribution of SST (unit: °C; color) in the BoB during the cyclogenesis season for **a**) 2002–2011 and **b**) 2012–2021, and **c**) their differences. The dotted areas pass the significance test at 90% confidence level

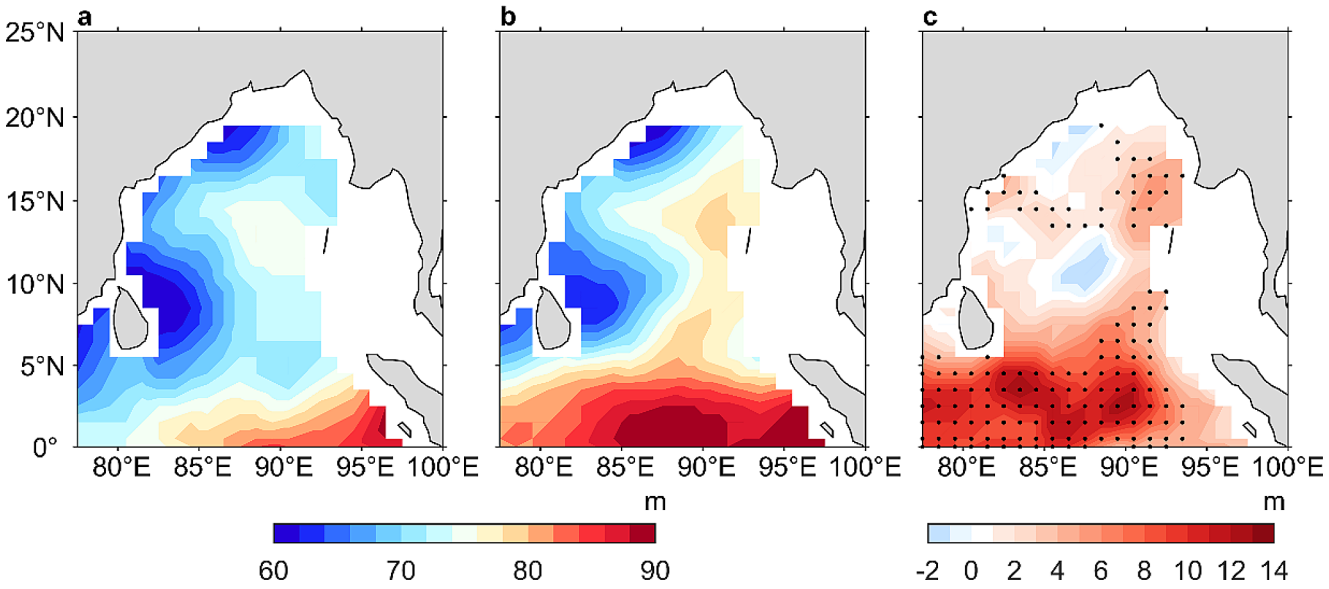

Fig. 10 Spatial distribution of D26 (unit: m; color) in the BoB during the cyclogenesis season for **a)** 2002–2011 and **b)** 2012–2021, and **c)** their differences. The dotted areas pass the significance test at 90% confidence level

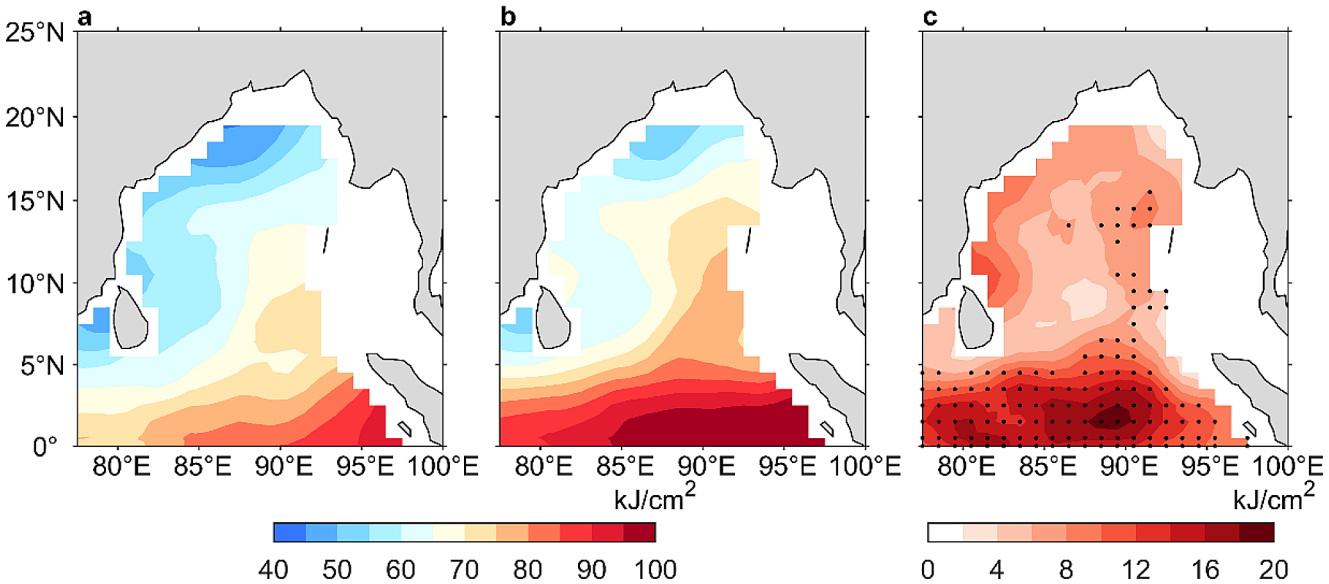

Fig. 11 Spatial distribution of UOHC (unit: kJ/cm^2; color) in the BoB during the cyclogenesis season for **a)** 2002–2011 and **b)** 2012–2021, and **c)** their differences. The dotted areas pass the significance test at 90% confidence level

downwelling Kelvin waves that deepen the thermocline and increase UOHC. These waves travelled through the east coast and radiated westward Rossby waves, increasing the UOHC in the BoB (Balaguru et al. 2014; Girishkumar et al. 2011, 2013; Han 2005). The kinetic energy of the storms is primarily derived from the UOHC (Lin et al. 2008; Mainelli et al. 2008; Vissa et al. 2013; Wada and Usui 2007; Wada et al. 2012). The storms in the second period benefited from the positive UOHC anomalies along the SNP. The peak ceiling of the storm intensity increased, leading to an increase in the proportion of STCs.

4.2.4 Barrier layer thickness

The barrier layer functions as a barrier to heat exchange between the mixed layer and the thermocline, maintaining a high SST and UOHC and thereby influencing the storm intensity. As shown in Fig. 12, in the BoB, the occurrence rate of the barrier layer (positive zone) was quite high, and most areas had a BLT of 1 to 2 m. It was found that an irregular variation occurred in the BoB between the two decades (Fig. 12c). Thickening mainly occurred in the offshore area and the west-central BoB. In the other areas, the BLT was

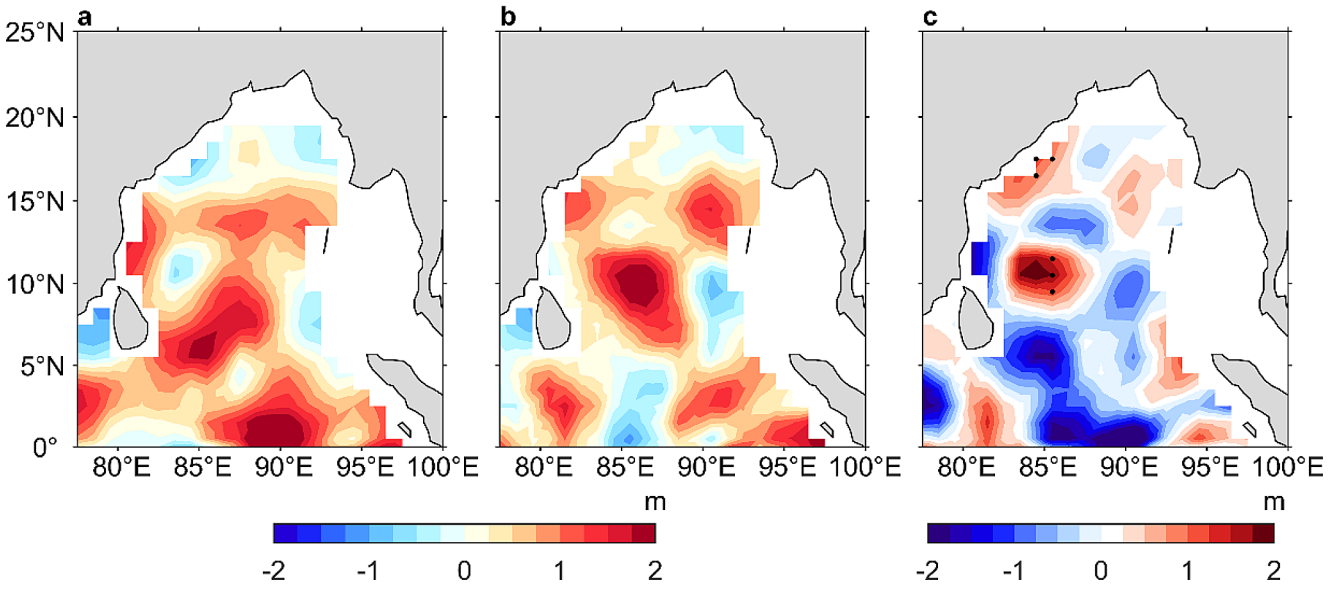

Fig. 12 Spatial distribution of BLT and CLT (unit: m; color) in the BoB during the cyclogenesis season for **a)** 2002–2011 and **b)** 2012–2021, and **c)** their differences. In **a)** and **b)**, positive values mean there is barrier layer in the seawater, while negative values mean there is compensated layer. The dotted areas pass the significance test at 90% confidence level

thinner, particularly in the southeast of Sri Lanka. The significantly thickened barrier layer along the northwestern coast could protect the SST from being cooled down under the effects of the entrainment of the storms, making it more likely that the storms would make landfall with greater intensity and destructiveness.

4.2.5 Air-sea heat fluxes

Affected by the sea surface wind, latent heat is absorbed via surface evaporation and then transported into the air. Once water vapor condenses and releases latent heat, the air is heated and lifted up, thereby enhancing the convection. The temperature difference between the sea and air can induce sensible heat transport. Both represent the quantity of heat exchange between the air-sea interface and play important roles in strengthening tropical cyclones by transforming heat energy into kinetic energy (Sun et al. 2016, 2020). As shown in Fig. 13a, b, d and e, in general, the air-sea heat fluxes were positive in the BoB, suggesting that the ocean transported heat into the atmosphere constantly during the cyclogenesis season. The upward heat transport was more obvious in the western and northern parts of the BoB, especially around the mouth of the bay. There were less latent heat fluxes around Sumatra. Figure 13c and f show the differences between the two decades. It can be seen that the latent heat fluxes improved on the equator west of 94°E, north of 10°N to the west of the Andaman Islands, and north of 13°N to the east of the Andaman Islands. The positive anomaly center exceeded 30 W/m^2 and was located in the mouth of the bay. The area from 13°N to south of the Andaman Sea was a negative area, and it expanded westward to Sri Lanka at 5−10°N. In terms of sensible heat fluxes, they increased north of 5°N in the ocean, which was consistent with areas exhibiting a sea-air temperature difference change of more than 0.1 °C (Fig. 14c).

Earlier studies decomposed the latent heat flux into components associated with surface wind speed and sea-air humidity difference (Small et al. 2019; Sun and Wu 2022). Consequently, further investigation was conducted into the changes in these two variables, as illustrated in Fig. 14a−b. It can be observed that over the northeastern coast of the BoB, the surface wind speed increased by 0.3 m/s during the second decade, and the sea-air humidity difference improved by 0.1 to 0.4 g/kg over the northern BoB. As a result, regions where these two areas overlapped exhibited higher upward latent heat transport (Fig. 13c). In the northwestern BoB focused on in this study, it was the increase in sea-air humidity difference that primarily led to the enhanced latent heat transport. Additionally, a greater temperature difference between the sea and air occurred in north of 5°N, especially along the rim of the BoB (Fig. 14c), facilitating sensible heat transport (Fig. 13f). These changes indicate a warmer, moister lower atmosphere in the latter decade. The SNP was present in the area where the heat flux supply was enhanced, and therefore, it was easier for the storms in this area to develop convection and to intensify into STCs.

4.2.6 Specific humidity

The analysis of the oceanic elements revealed that the warming of the upper ocean during 2012–2011 provided

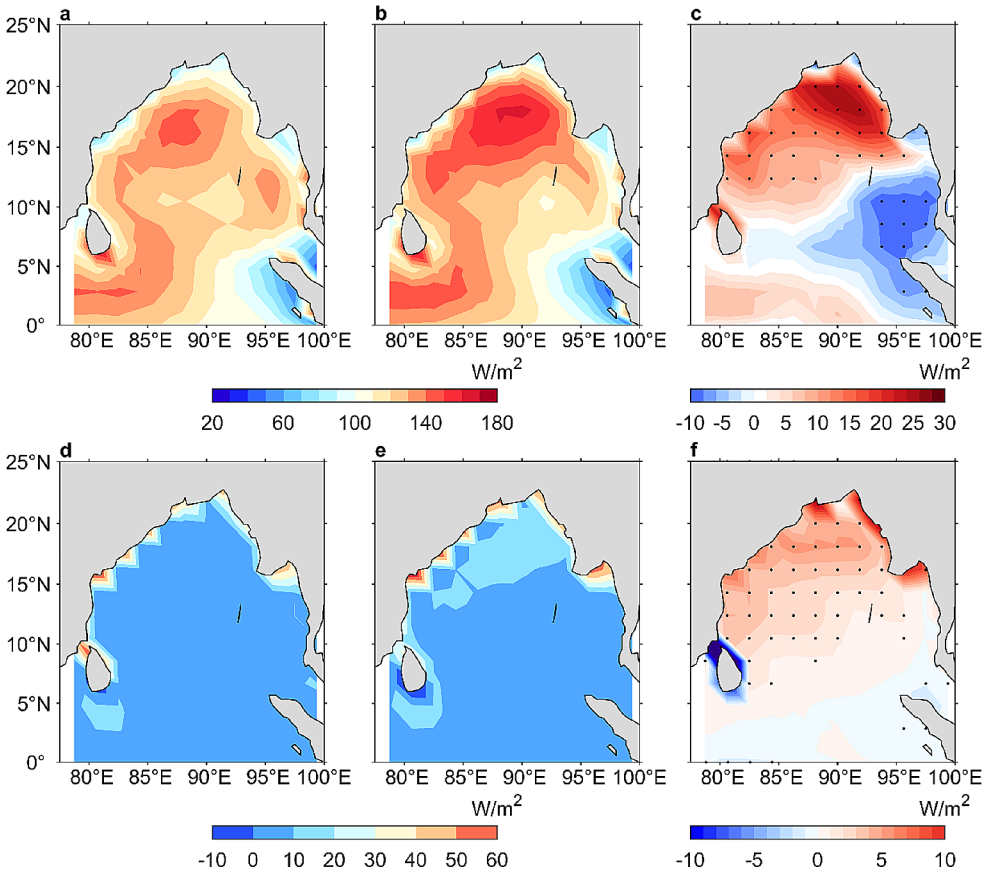

Fig. 13 Spatial distribution of **a–c)** latent heat fluxes and **d–f)** sensible heat fluxes (units: W/m^2; color). in the BoB during the cyclogenesis season for **a)** 2002–2011 and **b)** 2012–2021, and **c)** their differences. In **a)**, **b)**, **d)** and **e)**, positive values mean that heat is transported upward (from the sea to the air), and negative values mean that heat is transported downward (from the air to the sea). The dotted areas pass the significance test at 90% confidence level.

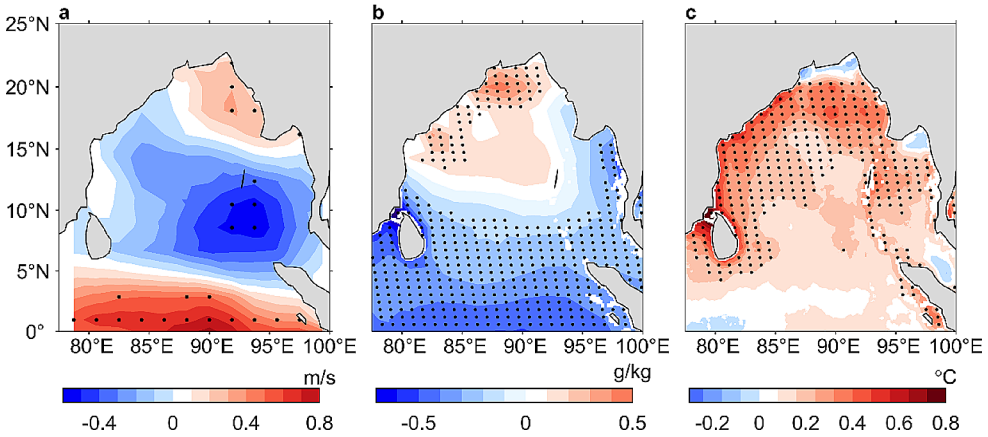

Fig. 14 Changes in mean **a**) 10-meter height wind speed (units: m/s; color), **b**) sea-air humidity difference (unit: g/kg; color) and **c**) sea-air temperature difference (units: °C; color) between 2012–2021 and 2002–2021. The dotted areas pass the significance test at 90% confidence level

plenty of energy for the intensification of the storms. It is also important to determine if the atmospheric conditions were favorable. The water vapor content at the middle and low troposphere is important to the growth of storms. Figure 15 depicts the SH at the 850 hPa pressure level during the two decades and the difference between the decades. The atmosphere over the mouth of the BoB was drier with an SH of around 7 g/kg, while the SH was higher over the equator, especially near Sumatra where the SH exceeded 10 g/kg. Between the two decades, it was found that the low SH area moved from the Indian coast to the Bangladesh coast. The SH decreased by 0.1–0.5 g/kg along the northeastern coast and increased by 0.2–0.5 g/kg in other areas, which was consistent with the change in the storm frequency distribution. It can be concluded that the wetter middle and lower troposphere over the northwestern BoB provided favorable conditions for storm intensification.

4.2.7 Vertical wind shear

The VWS during the two decades and the difference between the two decades are depicted in Fig. 16. Strong

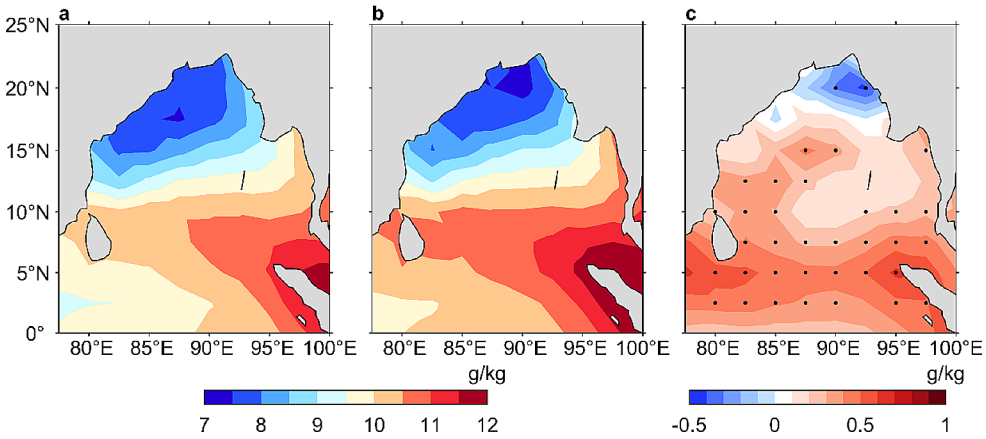

Fig. 15 Spatial distribution of the SH at the 850 hPa pressure level (units: g/kg; color) in the BoB during the cyclogenesis season for **a)** 2002–2011 and **b)** 2012–2021, and **c)** their differences. The dotted areas pass the significance test at 90% confidence level

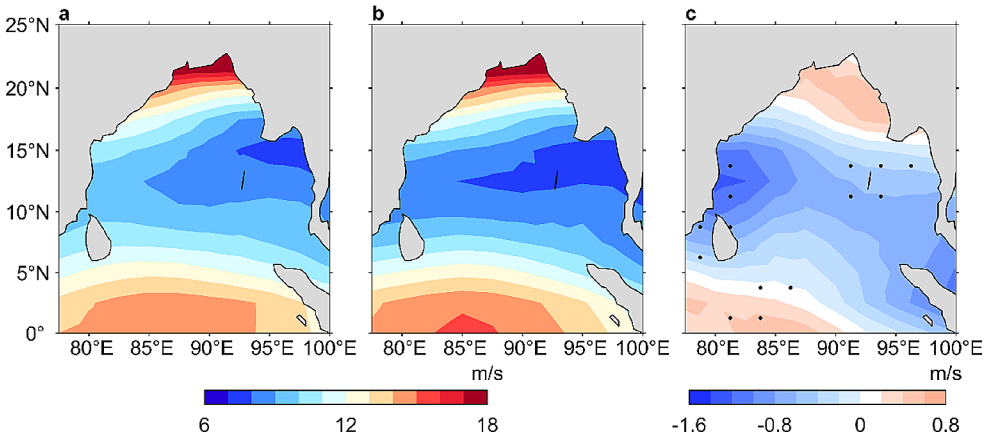

Fig. 16 Spatial distribution of the VWS (units: m/s; color) in the BoB during the cyclogenesis season for **a)** 2002–2011 and **b)** 2012–2021, and **c)** their differences. The dotted areas pass the significance test at 90% confidence level

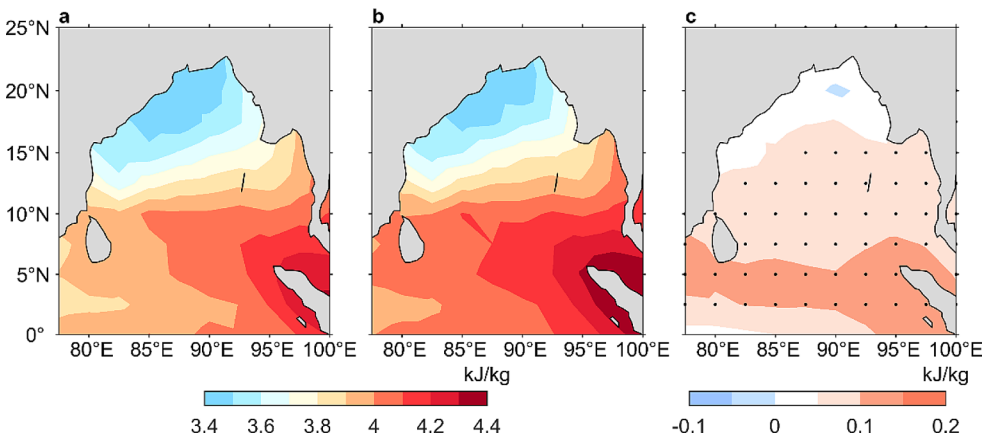

Fig. 17 Spatial distribution of the MSE between the 700 hPa and 925 hPa pressure levels (units: kJ/kg; color) in the BoB during the cyclogenesis season for **a)** 2002–2011 and **b)** 2012–2021, and **c)** their differences. The dotted areas pass the significance test at 90% confidence level

VWS occurred over the mouth of the Bay and the equator, whereas the VWS was weaker in the central region, especially in the eastern BoB. During 2012–2021, the SNP was situated within a large southeast-northwestward negative VWS anomaly. Thereby, it was easier for the storms generated during this period to accumulate moisture and heat within a confined space, and it increased the possibility of the storms growing into STCs.

4.2.8 Moist static energy

In South Asia, moisture is a primary factor influencing the MSE (Adames and Ming 2018). Consequently, the MSE reflects the potential release of latent heat during bursts of atmospheric convection in the BoB, which plays an important role in the sustained intensification of storms (Prakash et al. 2022). Figure 17 shows the MSE between the 700 hPa and 925 hPa levels during the two decades and the difference between the two decades. Over the BoB, the MSE was greater near the equator and Sumatra, and the lowest

values occurred over the mouth of the bay. There was a general increase in the MSE during 2012–2021, with larger increases at lower latitudes. The enhanced atmospheric instability made a significant positive contribution to the vertical ascent of air parcels, leading to more severe convection. With a constant supply of moisture from the convergence of the large-scale steering flow, the convection continued to deepen, which in turn facilitated the cyclonic circulation. This positive feedback mechanism was the conditional instability of the second kind (CISK) (Charney and Eliassen 1964), which contributed to the storm intensification in the BoB.

5 Summary and discussion

In this study, we investigated the changes in the storm activity over the BoB during 2002–2021 and the reasons for these changes. By comparing the spatial distribution of the quantity of storm centers during 2002–2011 and 2012–2021, it was found that an increase in the number of storm centers occurred in the northwestern BoB during the second decade. This led to the appearance of an SNP, which was narrow in Q4 and wide in Q2. In addition, more STCs occurred during the second decade and most of these STCs were located in the SNP. To confirm these changes, statistical analyses were conducted on the storm characteristics over the two decades. The longitudes and latitudes at which storms reached their LMIs decreased by −0.15° per year and increased by 0.1° per year, respectively, indicating northwestward migration of the storm LMIs. The LMIs increased consistently over the two decades at a rate of 1.73 kt per year. The mean translation direction of the storms exhibited a west-northwest change, which was consistent with the trends of the LMI positions. The total frequency and duration remained roughly the same between the two decades, but the occurrences and durations of the STCs increased sharply. The translation speed of the storms decreased, which may have caused the increase in the storm duration. The annual ACE of the storms with an intensity of ≥ 34 kt in each quadrant was also calculated. The results showed that the ACEs in Q1 and Q2 were mainly from STC centers, while the ACEs in Q3 and Q4 were derived from TC centers. During 2002–2011, the ACE was much greater in Q1 than in Q2, whereas the situation was reversed in the second decade due to the migration of the STC centers from Q1 to Q2. The increased ACE in Q2 was also sourced from TC centers in Q3, which transformed into STC centers after entering Q2. These two sources contributed primarily to the enhanced ACE in Q2.

The evolution of the steering flow and the environmental conditions played crucial roles in the motion and intensification of the storms. During 2012–2021, the asymmetrical increasing pattern of H_{500} modulated by the negative-to-positive phase change of the PDO contributed to the evolution of the large-scale steering flow. As a result, a CCA appeared in Q3 and an ACA anomaly appeared in Q1. Pushed by the southeast anomaly between the two circulation anomalies, the storms entered the SNP and moved northwestward. Along the SNP, the higher SST and UOHC supplied additional heat to the storms. The thicker warm water layer and barrier layer weakened the cooling effects of the upper ocean's response to the storms. The increased upward heat fluxes at the air-sea interface, the moisture and instability within the lower troposphere, and the reduced vertical wind shear in the SNP collectively facilitated the development of convection within the storm systems. These favorable factors improved the potential of storm development into STCs and increased the risk of the northwestern BoB being impacted by more destructive storms.

Having identified the possible causes of the increasing impacts of tropical cyclones on the northwestern BoB, it is important to determine whether these changes are part of a long-term trend or are a decadal variation. Limited to the timespan of the dataset, we only made an additional investigation of the storm tracks and intensities 20 years before the study period. It was found that of the 30 storms during 1982–1991, 24 were TCs and six were STCs, while in the subsequent decade (1992–2001), of the 28 storms, nine were TCs and 19 were STCs. Notably, during the decades with higher occurrences of STCs, there was an increase in the quantity of storms that moved towards the northwestern BoB. Conversely, in the decades with lower occurrences of STCs, there was a gap in the storm activity within the northwestern region, and the tracks of the STCs predominantly moved in a westward or northeastern direction. This is an interesting phenomenon and suggests that the ratio of TCs to STCs in the BoB and the tracks of the STCs may exhibit a decadal variation. The occurrence of the SNP was likely influenced by the decadal changes in the large-scale environment in the BoB, which was closely linked to phase conversion of several climate modes such as the PDO. The relationship between the natural variability, climate modes, and changes in storm events remains to be further investigated in the future.

Acknowledgements The authors thank the JTWC, NOAA, RSS, CARDC, TCC, NCEP/NCAR, and EM-DAT for providing the datasets employed herein. This work was supported by the National Natural Science Foundation of China (42376030), the Natural Science Foundation of Shandong Province (ZR2022MD020, DKXZZ202206), the Basic Scientific Fund for the National Public Research Institutes of China (2020Q05) and the Youth Science Foundation Project of the East China Sea Bureau, Ministry of Natural Resources (202205).

Author contributions D.W., X.J. and J.S.; Methodology: D.W., X.J. and X.H.; Formal analysis: D.W., X.J. and J.S.; Investigation: D.W.

and X.J.; Writing-original draft preparation: D.W.; Writing-review and editing: X.J. and J.S.; Funding acquisition: J.S.; Resources: J.S. and X.X.; Supervision: X.X. All authors commented on previous versions of the manuscript. All authors read and approved the final manuscript.

Funding This work was supported by the National Natural Science Foundation of China (42376030), the Natural Science Foundation of Shandong Province (ZR2022MD020, DKXZZ202206), the Basic Scientific Fund for National Public Research Institutes of China (2020Q05) and the Youth Science Foundation Project of the East China Sea Bureau, Ministry of Natural Resources (202205).

Data availability The datasets used for this work are publicly available and can be obtained from the following sources: IBTrACS made by NOAA NCDC (https://www.ncei.noaa.gov/products/international-best-track-archive, accessed on 13 February 2023), SST data from RSS (https://www.remss.com/measurements/sea-surface-temperature/, accessed on 10 January 2023), Argo data provided by the China Argo Real-time Data Center (http://www.argo.org.cn/index.php?m=content&c=index&a=lists&catid=27, accessed on 6 December 2022), atmospheric data reanalyzed by NCEP/NCAR (https://psl.noaa.gov/data/gridded/data.ncep.reanalysis.html, accessed on 13 February 2023), PDO index provided by the Tokyo Climate Center, Climate Prediction Division (https://ds.data.jma.go.jp/tcc/tcc/products/elnino/decadal/pdo_month.html, accessed on 5 November 2023), economic losses and human casualties compiled by EM-DAT (www.emdat.be, accessed on 17 May 2023), Etopo2 Dataset provided by the National Geophysical Data Center (https://www.ncei.noaa.gov/products/etopo-global-relief-model, accessed on 1 December 2022).

Declarations

Competing interests The authors have no relevant financial or non-financial interests to disclose.

References

Adames ÁF, Ming Y (2018) Moisture and moist static energy budgets of south Asian monsoon low pressure systems in GFDL AM4.0. J Atmos Sci 75:2107–2123. https://doi.org/10.1175/JAS-D-17-0309.1

Balaguru K, Taraphdar S, Leung LR, Foltz GR (2014) Increase in the intensity of Postmonsoon Bay of Bengal tropical cyclones. Geophys Res Lett 41:3594–3601. https://doi.org/10.1002/2014GL060197

Camargo SJ, Sobel AH (2005) Western North Pacific tropical cyclone intensity and ENSO. J Clim 18:2996–3006. https://doi.org/10.1175/JCLI3457.1

Chan KTF (2019) Are global tropical cyclones moving slower in a warming climate? Environ Res Lett 14:104015. https://doi.org/10.1088/1748-9326/ab4031

Charney JG, Eliassen A (1964) On the growth of the hurricane depression. J Atmos Sci 21:68–75. https://doi.org/10.1175/1520-0469(1964)021%3C0068:OTGOTH%3E2.0.CO;2

Chih C-H, Wu C-C (2020) Exploratory analysis of upper-ocean heat content and sea surface temperature underlying tropical cyclone rapid intensification in the Western North Pacific. J Clim 33:1031–1050. https://doi.org/10.1175/JCLI-D-19-0305.1

Cui W, Zhang J, Yang J (2022) Seasonal variation in eddy activity and associated heat/salt transport in the Bay of Bengal based on satellite, Argo, and 3D reprocessed data. Ocean Sci 18:1645–1663. https://doi.org/10.5194/os-18-1645-2022

Deshpande M, Singh V, Mano Kranthi G, Koll R, Rongmie E, Kumar U (2021) Changing status of tropical cyclones over the north. Indian Ocean Clim Dyn 57:3545–3567. https://doi.org/10.1007/s00382-021-05880-z

Dong X, Zeng G, Zhang G, Yang X (2023) Current AMO mitigating extreme high temperatures in Central Asia under global warming. Int J Climatol 43:3947–3962. https://doi.org/10.1002/joc.8066

Duan W, Yuan J, Duan X, Feng D (2021) Seasonal variation of tropical cyclone genesis and the related large-scale environments: comparison between the Bay of Bengal and Arabian Sea sub-basins. Atmosphere 12:1593. https://doi.org/10.3390/atmos12121593

Emanuel KA (1999) Thermodynamic control of hurricane intensity. Nature 401:665–669. https://doi.org/10.1038/44326

Emanuel KA, Nolan DS (2004) Tropical cyclone activity and the global climate system. Proc. of 26th Conference on Hurricanes and Tropical Meteorology, Miami, FL, American Meteorological Society

Feng J, Wang L, Chen W (2014) How does the east Asian summer monsoon behave in the decaying phase of El Niño during different PDO Phases? J Clim 27:2682–2698. https://doi.org/10.1175/JCLI-D-13-00015.1

Girishkumar MS, Ravichandran M (2012) The influences of ENSO on tropical cyclone activity in the Bay of Bengal during October–December. J Geophys Res: Oceans 117:C02003. https://doi.org/10.1029/2011JC007417

Girishkumar MS, Ravichandran M, McPhaden MJ, Rao RR (2011) Intraseasonal variability in barrier layer thickness in the south central Bay of Bengal. J Geophys Res: Oceans 116. https://doi.org/10.1029/2010JC006657

Girishkumar MS, Ravichandran M, Han W (2013) Observed intraseasonal thermocline variability in the Bay of Bengal. J Geophys Res: Oceans 118:3336–3349. https://doi.org/10.1002/jgrc.20245

Gray WM (1968) Global view of the origin of tropical disturbances and storms. Mon Weather Rev 96:669–700. https://doi.org/10.1175/1520-0493(1968)096%3C0669:GVOTOO%3E2.0.CO;2

Gray WM (1979) Hurricanes: their formation, structure and likely role in the tropical circulation. In: D.B.Shaw(ed) Meteorology over the Tropical oceans. Royal Meteorological Society, London, pp 155–218

Han W (2005) Origins and dynamics of the 90-day and 30–60-day variations in the equatorial Indian Ocean. J Phys Oceanogr 35:708–728. https://doi.org/10.1175/JPO2725.1

Hsu P-C, Chu P-S, Murakami H, Zhao X (2014) An abrupt decrease in the late-season typhoon activity over the western North Pacific. J Clim 27:4296–4312. https://doi.org/10.1175/JCLI-D-13-00417.1

Kabir R, Ritchie EA, Stark C (2022) Tropical cyclone exposure in the North Indian Ocean. Atmosphere 13:1421. https://doi.org/10.3390/atmos13091421

Kalnay E, Kanamitsu M, Kistler R et al (1996) The NCEP/NCAR 40-year reanalysis project. Bull Am Meteorol Soc 77:437–472.

https://doi.org/10.1175/1520-0477(1996)077%3C0437:TNYRP%3E2.0.CO;2
Kashem M, Ahmed MK, Qiao F, Akhter MA, Chowdhury KM (2019) The response of the upper ocean to tropical cyclone Viyaru over the Bay of Bengal. Acta Oceanol Sin 38:61–70. https://doi.org/10.1007/s13131-019-1370-1
Kim S-H, Moon I-J, Chu P-S (2020) An increase in global trends of tropical cyclone translation speed since 1982 and its physical causes. Environ Res Lett 15:094084. https://doi.org/10.1088/1748-9326/ab9e1f
Knapp KR, Kruk MC, Levinson DH, Diamond HJ, Neumann CJ (2010) The International Best Track Archive for Climate Stewardship (IBTrACS): Unifying Tropical Cyclone Data. Bull Am Meteorol Soc 91:363–376. https://doi.org/10.1175/2009BAMS2755.1
Knapp KR, Diamond HJ, Kossin JP, Kruk MC, Schreck CJI (2018) International Best Track Archive for Climate Stewardship (IBTrACS) project, v04r00. https://doi.org/10.25921/82ty-9e16.
Kossin JP (2018) A global slowdown of tropical-cyclone translation speed. Nature 558:104–107. https://doi.org/10.1038/s41586-018-0158-3
Kossin JP, Olander TL, Knapp KR (2013) Trend analysis with a new global record of tropical cyclone intensity. J Clim 26:9960–9976. https://doi.org/10.1175/JCLI-D-13-00262.1
Kossin JP, Emanuel KA, Vecchi GA (2014) The poleward migration of the location of tropical cyclone maximum intensity. Nature 509:349–352. https://doi.org/10.1038/nature13278
Krishnamohan KS, Mohanakumar K, Joseph PV (2012) The influence of Madden–Julian oscillation in the genesis of north Indian Ocean tropical cyclones. Theor Appl Climatol 109:271–282. https://doi.org/10.1007/s00704-011-0582-x
Leipper DF, Volgenau D (1972) Hurricane heat potential of the Gulf of Mexico. J Phys Oceanogr 2:218–224. https://doi.org/10.1175/1520-0485(1972)002%3C0218:HHPOTG%3E2.0.CO;2
Li Z, Yu W, Li T, Murty VSN, Tangang F (2013) Bimodal character of cyclone climatology in the Bay of Bengal modulated by monsoon seasonal cycle. J Clim 26:1033–1046. https://doi.org/10.1175/JCLI-D-11-00627.1
Li H, Xu F, Zhou W, Wang D, Wright JS, Liu Z, Lin Y (2017) Development of a global gridded Argo data set with Barnes successive corrections. J Geophys Res: Oceans 122:866–889. https://doi.org/10.1002/2016JC012285
Lin I-I, Wu C-C, Pun I-F, Ko D-S (2008) Upper-ocean thermal structure and the western North Pacific category 5 typhoons. Part I: ocean features and the category 5 typhoons' intensification. Mon Weather Rev 136:3288–3306. https://doi.org/10.1175/2008MWR2277.1
Liu KS, Chan JCL (2013) Inactive period of western North Pacific tropical cyclone activity in 1998–2011. J Clim 26:2614–2630. https://doi.org/10.1175/JCLI-D-12-00053.1
Liu Q, Zhou T, Mao H, Fu C (2019) Decadal variations in the relationship between the western Pacific subtropical high and summer heat waves in east China. J Clim 32:1627–1640. https://doi.org/10.1175/JCLI-D-18-0093.1
Mainelli M, DeMaria M, Shay LK, Goni G (2008) Application of oceanic heat content estimation to operational forecasting of recent Atlantic category 5 hurricanes. Wea Forecast 23:3–16. https://doi.org/10.1175/2007WAF2006111.1
McGillicuddy DJ (2015) Formation of intrathermocline lenses by eddy–wind interaction. J Phys Oceanogr 45:606–612. https://doi.org/10.1175/JPO-D-14-0221.1
Mohapatra M, Kumar VV (2017) Interannual variation of tropical cyclone energy metrics over North Indian Ocean. Clim Dyn 48:1431–1445. https://doi.org/10.1007/s00382-016-3150-3
Murakami H, Delworth TL, Cooke WF, Zhao M, Xiang B, Hsu P-C (2020) Detected climatic change in global distribution of tropical cyclones. Proceedings of the National Academy of Sciences 117:10706–10714. https://doi.org/10.1073/pnas.1922500117
National Geophysical Data Center (2006) 2-minute Gridded Global Relief Data (ETOPO2) v2. https://doi.org/10.7289/V5J1012Q
Neumann CJ (2017) A global tropical cyclone climatology. Global guide to Tropical Cyclone forecasting. World Meteorological Organization (WMO), Geneva, pp 28–62. https://library.wmo.int/index.php?lvl=notice_display&id=16963
Peduzzi P, Chatenoux B, Dao H et al (2012) Global trends tropical cyclones risk. Nat Clim Change 2:289–294. https://doi.org/10.1038/nclimate1410
Prakash KR, Pant V, Udaya Bhaskar TVS, Chandra N (2022) What made the sustained intensification of tropical cyclone Fani in the Bay of Bengal? An investigation using coupled atmosphere–ocean model. Atmosphere 13:535. https://doi.org/10.3390/atmos13040535
Qin W, Cai Y, He L (2024) The relationship between the typhoons affecting south China and the Pacific decadal oscillation. Atmosphere 15. https://doi.org/10.3390/atmos15030285
Sahoo B, Bhaskaran PK (2016) Assessment on historical cyclone tracks in the Bay of Bengal, east coast of India. Int J Climatol 36:95–109. https://doi.org/10.1002/joc.4331
Shan K, Yu X (2021) Variability of tropical cyclone landfalls in China. J Clim 34:1–26. https://doi.org/10.1175/JCLI-D-21-0031.1
Shrivastav A, Behboodi A, Sarkar-Swaisgood M, Dewi MB, K, Suman RK, Dubey S, Hong S (2022) Pathways to adaptation and resilience in south and south–west Asia, pp 67. https://www.unescap.org/kp/2021/asia-pacific-disaster-report-2021
Small RJ, Bryan FO, Bishop SP, Tomas RA (2019) Air–sea turbulent heat fluxes in climate models and observational analyses: what drives their variability? J Clim 32:2397–2421. https://doi.org/10.1175/JCLI-D-18-0576.1
Sreenivas P, Gnanaseelan C, Prasad K, V S R (2012) Influence of El Niño and Indian Ocean Dipole on sea level variability in the Bay of Bengal. Global Planet Change 80–81:215–225. https://doi.org/10.1016/j.gloplacha.2011.11.001
Sun X, Wu R (2022) Contribution of wind speed and sea-air humidity difference to the latent heat flux-SST relationship. Ocean-Land-Atmos Res 2022. https://doi.org/10.34133/2022/9815103.
Sun J, Zuo J, Ling Z, Yan Y (2016) Role of ocean upper layer warm water in the rapid intensification of tropical cyclones: a case study of typhoon Rammasun (1409). Acta Oceanol Sin 35:63–68. https://doi.org/10.1007/s13131-015-0761-1
Sun J, Wang G, Zuo J, Ling Z, Liu D (2017) Role of surface warming in the northward shift of tropical cyclone tracks over the South China Sea in November. Acta Oceanol Sin 36:67–72. https://doi.org/10.1007/s13131-017-1061-8
Sun J, Wang D, Hu X, Ling Z, Wang L (2019) Ongoing poleward migration of tropical cyclone occurrence over the western North Pacific Ocean. Geophys Res Lett 46:9110–9117. https://doi.org/10.1029/2019GL084260
Sun J, Wang G, Xiong X et al (2020) Impact of warm mesoscale eddy on tropical cyclone intensity. Acta Oceanol Sin 39:1–13. https://doi.org/10.1007/s13131-020-1617-x
Sun Y, Zhong Z, Li T, Yi L, Shen Y (2021) The slowdown tends to be greater for stronger tropical cyclones. J Clim 34:5741–5751. https://doi.org/10.1175/JCLI-D-20-0449.1
Sun J, Wang G, Jin S, Ju X, Xiong X (2022) Quantifying tropical cyclone intensity change induced by sea surface temperature. Int J Climatol 42:4716–4727. https://doi.org/10.1002/joc.7499
Tokyo Climate Center (2023) Monthly Pacific decadal oscillation (PDO) index. https://ds.data.jma.go.jp/tcc/tcc/products/elnino/decadal/pdo_month.html
Vissa NK, Satyanarayana ANV, Prasad Kumar B (2013) Intensity of tropical cyclones during pre- and post-monsoon seasons in relation to accumulated tropical cyclone heat potential over Bay

of Bengal. Nat Hazard 68:351–371. https://doi.org/10.1007/s11069-013-0625-y

Wada A, Usui N (2007) Importance of tropical cyclone heat potential for tropical cyclone intensity and intensification in the western North Pacific. J Oceanogr 63:427–447. https://doi.org/10.1007/s10872-007-0039-0

Wada A, Usui N, Sato K (2012) Relationship of maximum tropical cyclone intensity to sea surface temperature and tropical cyclone heat potential in the North Pacific Ocean. J Geophys Res Atmos 117:D11118. https://doi.org/10.1029/2012JD017583

Wahiduzzaman M, Yeasmin A (2020) A kernel density estimation approach of North Indian Ocean tropical cyclone formation and the association with convective available potential energy and equivalent potential temperature. Meteorol Atmos Phys 132:603–612. https://doi.org/10.1007/s00703-019-00711-7

Wentz FJ, Gentemann C, Hilburn KA (2015) Remote Sensing Systems TRMM TMI Daily Environmental Suite on 0.25 deg grid, Version 7.1, MW_IR OI SST Product. http://www.remss.com/missions/tmi

Wu L, Wang B (2004) Assessing impacts of global warming on tropical cyclone tracks. J Clim 17:1686–1698. https://doi.org/10.1175/1520-0442(2004)017%3C1686:AIOGWO%3E2.0.CO;2

Xu Y, Li T, Shen S, Hu Z (2019) Assessment of CMIP5 models based on the interdecadal relationship between the PDO and winter temperature in China. Atmosphere 10:597. https://doi.org/10.3390/atmos10100597.

Yanase W, Satoh M, Taniguchi H, Fujinami H (2012) Seasonal and intraseasonal modulation of tropical cyclogenesis environment over the Bay of Bengal during the extended summer monsoon. J Clim 25:2914–2930. https://doi.org/10.1175/JCLI-D-11-00208.1

Yang K, Cai W, Huang G, Hu K, Ng B, Wang G (2022) Increased variability of the western Pacific subtropical high under greenhouse warming. Proc Natl Acad Sci 119:e2120335119. https://doi.org/10.1073/pnas.2120335119

Yuan J, Cao J (2013) North Indian Ocean tropical cyclone activities influenced by the Indian Ocean Dipole mode. Sci China Earth Sci 56:855–865. https://doi.org/10.1007/s11430-012-4559-0

Zhang D, Huang Y, Zhou B, Wang H (2021) Is there interdecadal variation in the south Asian high? J Clim 34:8089–8103. https://doi.org/10.1175/JCLI-D-21-0059.1

Zhou X, Qiu Y, Lin X, Teng H, Aung C (2022) An intrathermocline eddy observed in the northeastern Bay of Bengal. Geophys Res Lett 49:e2022GL099201. https://doi.org/10.1029/2022GL099201.